Self-Seeding Synthesis of Hierarchically Branched Rutile TiO$_2$ for High-Efficiency Dye-Sensitized Solar Cells

Dongting Wang,* Yifan Hu, Yuchen Li, Xiangchen Jia, Yuzhen Fang, Zhiliang Zhang, and Xianxi Zhang

Cite This: *ACS Omega* 2023, 8, 9843−9853

Read Online

ACCESS | Metrics & More | Article Recommendations | Supporting Information

ABSTRACT: This study presents a unique and straightforward room temperature-based wet-chemical technique for the self-seeding preparation of three-dimensional (3D) hierarchically branched rutile TiO$_2$, abbreviated HTs, employing titanate nanotubes as the precursor. In the course of the synthesis, spindle-like rutile TiO$_2$ and the intermediate anatase phase were first obtained through a dissolution/precipitation/recrystallization process, with the former serving as the substrates and the latter as the nucleation precursor to growing the branches, which finally gave birth to the production of 3D HTs nanostructures. When the specifically created hierarchical TiO$_2$ was used as the photoanode in dye-sensitized solar cells (DSCs), a significantly improved power conversion efficiency (PCE) of 8.32% was achieved, outperforming a typical TiO$_2$ (P25) nanoparticle-based reference cell (η = 5.97%) under the same film thickness. The effective combination of robust light scattering, substantial dye loading, and fast electron transport for the HTs nanostructures is responsible for the remarkable performance.
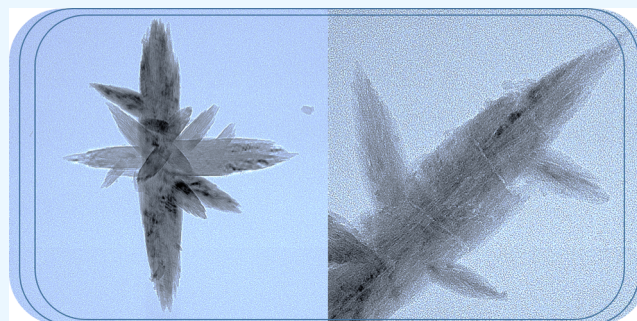
1. INTRODUCTION

Dye-sensitized solar cells (DSCs) stand out as one of the promising "next generation" optoelectronic devices due to their simple production techniques, low manufacturing cost, and chemical stability.[1−5] The heart of these solar cells is a TiO$_2$ nanomaterial photoanode, which not only supplies a high internal surface area for dye sensitizer adherence but also acts as the stable medium for photogenerated electrons delivery. Great attention has been therefore paid to controlling the crystal phase, shape, dimensions, and surface properties of nanostructured TiO$_2$ materials to construct outstanding photoanodes. TiO$_2$ has three different polymorphs: anatase, rutile, and brookite, and the TiO$_2$ rutile phase is prejudicially considered to be inferior to the anatase phase and thus often ignored in DSCs, mainly due to its more positive conduction band edge potential, which is regarded to be detrimental for the achievement of a higher open-circuit voltage in DSCs. Recent studies have, however, demonstrated that rutile TiO$_2$-based solar cell devices can also achieve a comparable V_{OC} to those made with anatase, and substantially enhanced electron transport has also been verified in one-dimensional (1D) rutile TiO$_2$ nanostructures, which largely eliminates the concerns of the researchers interested in rutile phase TiO$_2$.[6−8] Besides, rutile TiO$_2$ also possesses some superior physical properties over the anatase phase, especially the enhanced light-scattering properties in virtue of its higher refractive index, which is obviously beneficial from the perspective of efficient photon harvesting.[9,10] In this case, rutile TiO$_2$ is also an ideal candidate for a DSC device on the condition of taking full advantage of

its virtue and deliberately mitigating the drawbacks by elaborately tailoring the morphology features.

Various TiO$_2$ structures in the forms of nanotubes, nanorods, nanowires, nanofibers, nanosheets, and nanoflowers have been reported.[11−18] In comparison with the randomly organized network, though one-dimensional (1D) nanomaterials could offer fast electron transport highways, the fundamental drawbacks of a low internal surface area and the large void spaces between adjacent nanostructures become the main factors hindering performance improvement. Alternatively, three-dimensional (3D) hierarchical TiO$_2$ architectures consisting of 1D building blocks have attracted researchers' considerable attention since the elaborately designed nanostructures could often simultaneously functionalize integration of the virtues of lower dimensional structures, such as zero-dimensional (0D) and 1D nanomaterials, which thus provides the greatest possibility of improving the photovoltaic performance.[19−22] However, in many cases, the formation mechanism of these well-designed hierarchical structures is far less understood and sometimes even not considered, which thus is still an urgent issue to be tackled in this field.

Up to now, several techniques, including vapor deposition,[23] pulsed-laser deposition,[24] and atomic layer deposition (ALD),[25] template,[26,27] and hydrothermal methods,[28−30] have already been employed for the synthesis of hierarchically structured TiO_2 with controlled morphologies and architectures. As a consequence, all of these methods have been proven to be effective in manipulating the performance of the cells fabricated with the resultant hierarchical TiO_2. Nevertheless, the rigid demand for special instruments, solvents, and operating conditions, such as a high power supply reactor, high thermal treatment temperature, and designated template sources, not only increases the cost of the preparation process but also makes it hard to observe the concrete phase and morphology evolution of the precursors during the reaction. In addition, the structures obtained via the above methods are ordinarily subjected to complicated multiple-step processes, in which 1D nanostructures are generally synthesized in the first step, followed by immersing the as-prepared 1D nanostructure in the seeding solution to grow various desired structures on their surfaces. In this regard, preparing the 3D hierarchical structures through a more facile and straightforward synthetic method is urgently desirable. Different from many other methods, the room temperature-based synthesis process is simple yet effective since it is usually carried out under a normal atmosphere in a sealed or unsealed reactor, and under such a condition, it is convenient to observe the change of the reactants and precisely control the shape and crystallinity of the final product by regulating the reaction conditions such as pH, concentration, and the type of the precursors. Nevertheless, to the best of our knowledge, the synthesis of 3D hierarchical TiO_2 using a room temperature-processed one-step approach has yet to be reported.

Herein, a room temperature-based facile method was designed to produce an innovative 3D rutile TiO_2 nanostructure using titanate nanotubes as a precursor, in which the synthesized one-dimension spindle-like TiO_2 acted as substrates for the subsequent growth of the branches by a self-seeding process. During the process, the dissolution of the titanate nanotube first occurred, leading to the gradual formation of spindle-like TiO_2 accomplished by the crystal phase transformation from titanate to anatase TiO_2 and then to rutile TiO_2. Continuously extending the acid treatment time directly gave rise to the formation of the Ti precursor of TiO_2 branches, which finally led to the generation of the intriguing 3D rutile TiO_2 nanostructure. The DSCs assembled with the resultant hierarchical TiO_2 architecture as photoanodes delivered a short-circuit current intensity of 16.0 mA cm^{-2} and an open-circuit voltage of 0.743 V, resulting in an outstanding overall PCE of 8.32%, remarkably higher than that of the originally raw material P25 TiO_2, which merely displayed an efficiency of 5.97%. Various characterizations demonstrated that the improvement of the photovoltaic performance in such a hierarchical TiO_2 architecture was primarily due to the effective combination of the desired features of an excellent photoanode, i.e., large surface area, enhanced light-scattering capability, and high electron transport properties.

2. EXPERIMENTAL SECTION

2.1. Materials. The fluorine-doped tin oxide (FTO, sheet resistance 7 Ω^{-2}) glasses were received from Yingkou OPV Tech Co., Ltd. Commercial TiO_2 powder, P25 (Degussa AG, Germany), consisting of mixed phases of 80% anatase and 20% rutile, was obtained from Degussa (Germany). The Ru-based dye (N719) was purchased from Solaronix (Aubonne, Switzerland). All other chemicals, such as sodium hydroxide, hydrochloric acid, titanium tetrachloride, and ethanol, were of the analytical grade and employed as received without any purification.

2.2. Preparation of Hierarchically Branched Rutile TiO_2 (HTs). TiO_2 nanotubes were synthesized through a traditional hydrothermal method similar to the initial work by Kasuga and co-workers, followed by a room temperature-based aging process.[31−33] Specifically, 2 g of the P25 powder was put into a beaker (100 mL) containing 40 mL of the 10 M NaOH aqueous solution and stirred for 2 h to get a homogeneously dispersed white suspension. The specimen was then transferred into a Teflon vessel with an inner volume of 100 mL, sealed outside by a stainless steel autoclave, and then hydrothermally treated at 160 °C for 12 h in an electric oven. After the treatment, the resultant white precipitate in the autoclaved mixture was subjected to a sufficient washing treatment with deionized water until the pH value of the solution reached 12, followed by the gradual addition of the 2 M HCl aqueous solution until a desired acid pH value of 1 was reached. The obtained suspension with a volume of about 300 mL was transferred into a 500 mL beaker and kept at room temperature to yield HTs precipitates. After aging for 60 days, the resultant sample was ultimately collected by centrifugation and rinsed with deionized water four times by dispersing the wet precipitate into water via ultrasonication and recovering the solid by centrifugation. The wet white precipitate was then dried at 60 °C for 16 h to yield the white powder of hierarchically branched rutile TiO_2.

2.3. Preparation of HTs Photoanodes. The fabrication of photoanodes started from the preparation of a vicious TiO_2 paste by mixing hierarchically branched rutile TiO_2 (0.2 g), anhydrous ethanol (2 mL), ethyl cellulose (0.01 g), terpineol (0.6 g), and acetic acid (0.04 mL) together, followed by grounding for about 60 min. Fluorine-doped tin oxide (FTO)-conducting glass substrates (Nippon Sheet Glass (NSG), 7 Ω sq^{-1}) were pretreated sequentially in acetone, ethanol, and water for 30 min, respectively. Afterward, the resultant TiO_2 paste was coated uniformly on the FTO substrate using a typical doctor-blading method and dried at 80 °C for 8 h. Following the above protocol, the fabricated TiO_2 film was heated to 450 °C at the rate of 3 °C/min and maintained for 1 h to remove the organic residues. To deposit tiny TiO_2 crystallites on the HTs photoanode film, titanium tetrachloride ($TiCl_4$) was selected as a precursor and hydrolyzed at 77 °C for 50 min. After treatment, the TiO_2 film was rinsed with deionized water and ethanol and then heated at 500 °C for 60 min. For performance optimization, the thickness of HTs films was controlled by layers of adhesive tape, and HTs films with a thickness of approximately 5.6, 10.8, and 15.7 μm were fabricated, respectively. For comparison, a commercial TiO_2 (P25) photoanode was also fabricated according to the same process mentioned above.

2.4. Solar Cell Fabrication. Prior to device assembly, the as-received oxide electrodes were sensitized with a 5.0×10^{-4} M ruthenium complex [cis-bis(isothiocyanate)bis (2,2-bipyridyl-4,4-dicarboxylate) ruthenium(II) bis-(tetrabutylammonium)] (commercially known as N719) in ethanol for 24 h at room temperature and then rinsed with ethanol so as to remove unanchored dye molecules and dried naturally in air. The Pt-coated counter electrode was prepared

by pyrolysis of the H_2PtCl_6 solution (0.35 mM) in isopropyl alcohol spread on the FTO glass. The dye-anchored working electrode was assembled with the Pt-coated FTO counter electrode to construct a face-to-face cell device using an adhesive hot-melt film as a separating layer (25 μm). The redox electrolyte (0.12 M I_2, 1.0 M DMPII, 0.1 M LiI, and 0.5 M *t*-BPy in 3-methoxypropionitrile) was injected from one side of the open cell and then filled the whole active space (0.25 cm^2) by vacuum backfilling.

2.5. Material Characterization and Photoelectrochemical Measurements. The microstructure of hierarchically branched rutile TiO_2 was examined using scanning electron microscopy (FIB-SEM, Helios G4CX) and high-resolution transmission electron microscopy (HRTEM, Talos F200 X). The crystallographic information of samples was identified by powder X-ray diffraction (XRD, X′ Pert PRO MPD, PANalytical). The Brunauer–Emmett–Teller (BET) surface area was characterized using a Micromeritics Analyzer (ASAP-2460). The light absorption and reflectance spectra of samples were measured by UV–vis diffuse reflectance spectroscopy (UH4150, Hitachi) in the range of 200–800 nm. The measurement of the dye loading amount was conducted by first desorbing the absorbed sensitizer into 1.0 M NaOH in a water/ethanol (50:50, V/V) solution, followed by detecting the absorbance of the dye solution using a UV–vis spectrophotometer. The thickness of the resultant HTs films was determined using a KLA Tencor Alphastep D100 profilometer. The incident photon-to-current conversion efficiency (IPCE) spectra of the resultant DSCs were collected with a photovoltaic (PV) measurement QEX10 instrument. The photocurrent density–voltage (J–V) curves of the assembled DSCs were recorded using a Keithley Model 2400 digital source meter (Keithley) under AM 1.5 simulated one sun condition with an output power density of 100 mW cm^{-2}. EIS analysis was conducted through an electrochemical workstation (CHI760, CH Instruments) at an open-circuit voltage (V_{OC}) under 100 mW cm^{-2} illumination with an AC amplitude value of 10 mV and a frequency range of 0.1–10^6 Hz, respectively.

3. RESULTS AND DISCUSSION

3.1. XRD Analysis. The XRD characterization of the hierarchical TiO_2 is first performed and the corresponding result is presented in Figure 1a. The XRD pattern reveals that the rationally designed branched 3D structure could be indexed as pure rutile TiO_2 (JCPDS no. 21-1276; also see the XPS spectra shown in Figure S1) with the most substantial diffraction peaks at a 2θ value of approximately 27.4° and at the same time demonstrates that highly crystallized rutile TiO_2

could be achieved even by treating the H-titanate nanotube precursor at room temperature. Previous studies have pointed out that the transformation from H-titanate nanotubes to a less stable phase, i.e., anatase, could readily take place by hydrothermal treatment or direct calcination processes.[34,35] However, the further transformation of anatase into rutile seems more rigid, and the anatase structure can be maintained even after the calcination temperature reaches up to 700 °C. A similar result was also observed when the as-prepared H-titanate nanotubes were calcined at a temperature range of 600–800 °C in our experiment (see Figure S2a). On the other hand, Zhu et al. reported that another H-titanate precursor, namely, nanofibers, could directly convert to rutile crystals by treating the sample with a concentrated acid solution. Liu et al. suggested that the phase transitions from a titanate nanotube precursor to anatase and a titanate nanotube precursor to rutile occurred independently in the hydrothermal process.[36] In this context, the question now arises as to whether as-synthesized rutile TiO_2 is directly deduced from H-titanate during the room temperature-based reaction process or subjected to an intermediate phase similar to the feature of calcining titanate at high temperatures.

To gain insight into the phase transition, a time-dependent study of the phase composition was conducted. The crystalline features of the products obtained after aging at dissimilar times at room temperature were determined by XRD and are shown in Figure 1b. As noted in Figure 1b, two broader peaks located at 2θ of approximately 24.5 and 48.4° are observed for the sample acid-treated for 1 day. According to the previous literature, the sample can be indexed to layered hydrogen titanate ($H_2Ti_3O_7$, JCPDS no. 41-1092), with typical peaks corresponding to the reflection from (110) and (020) planes, respectively.[37−39] After aging for 10 days, the crystal composition changed significantly; the peaks corresponding to titanate vanished, and the diffraction peaks matched with anatase TiO_2 (JCPDS no. 21-1272) appeared, indicating the rapid rearrangement from H-titanate to the anatase phase. Such a transition could probably be ascribed to the dehydration of H-titanate and the structural unit (i.e., zigzag ribbons) rearrangement, which provides us the opportunity to readily exert control on the phase composition of titanate nanotubes via a room temperature-based wet chemistry reaction route.[40,41] As the reaction proceeded (20 days), these peaks assigned to the anatase phase all became sharper, indicating the further crystallization of the anatase TiO_2 product during the period. Strikingly, a small amount of rutile is also detected in addition to the predominant anatase phase when the reaction time is extended. Progressively, the intensity of diffraction peaks regarding anatase TiO_2 begins to decrease when the reaction time is continuously extended to 40 days, whereas the diffraction peaks corresponding to rutile grow more intensive concerning that of the sample treated for 20 days, which suggests that the gradual increase of the rutile phase fraction is at the cost of the anatase phase during this stage. Given the difference in the XRD patterns between the samples treated for 20 and 40 days, it is reasonable to conclude that rutile TiO_2 is formed via a consecutive phase evolution from H-titanate to anatase and then to rutile under the mild room temperature-based conditions. The significance of these findings lies in the fact that rutile phase TiO_2 is rarely directly prepared by ambient treatment of titanate nanotubes in acidic conditions and, more importantly, the transition of anatase to rutile at room temperature has not been achieved up to now.
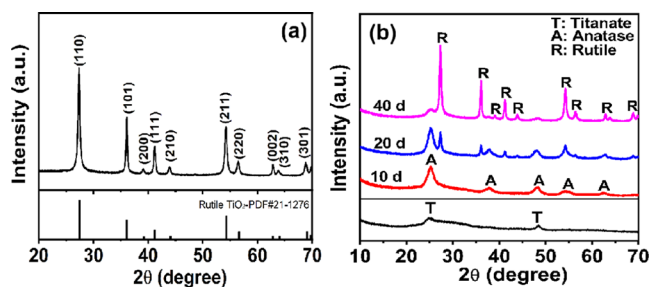

Figure 1. (a) XRD patterns of the obtained HTs and (b) the products prepared after treating the titanate precursor at different times.

The distinguishing phase transition could be mainly associated with the elaborately selected initial pH value of the acidic aqueous solution. As shown in Figure S2b, when the titanate precursor was treated with a 0.01 M HCl aqueous solution, the diffraction peaks assigned to titanate showed only negligible variation even after 60 days, further demonstrating the significant influence of acidic conditions.

3.2. Morphological Characterization of As-Synthesized TiO₂. Figure 2 displays the representative images of as-
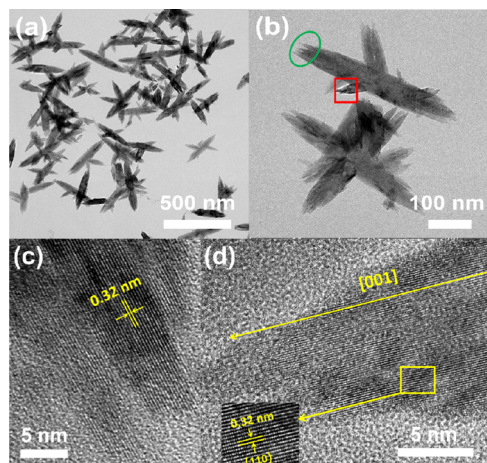

Figure 2. (a, b) Low-magnification TEM images of HTs and (c, d) high-resolution TEM images of the tips of both the substrate and branch in the HTs structure corresponding to the regions of selected parts in panel (b).

synthesized TiO₂ acquired from transmission electron microscopy (TEM) and high-resolution transmission electron microscopy (HRTEM). As seen in Figure 2a, as-prepared TiO₂ showed a typical 3D branched hierarchical morphology; the spindle-like structure was approximately 500 nm in length and the sharp branch was in the range of 50−300 nm. The morphological feature was further verified by the magnified TEM image shown in Figure 2b. Figure 2c shows the lattice-resolved HRTEM images of the HTs sample. From a distance

between lattice fringes, an estimated interplanar spacing of 0.32 nm was obtained for the substrate, which was exactly consistent with the d value of the (110) lattice spacing of rutile TiO₂, suggesting that spindle-like rutile TiO₂ preferably grew along the [001] direction.[42] Interestingly, the same crystalline distance, i.e., $d_{110} = 0.32$ nm, was obtained for the lateral branches (see Figure 2d), which demonstrates that branched TiO₂ was grown onto the one-dimensional substrate also along the [001] axis.

To shed light on the detailed structure evolution process of such interesting branched hierarchical rutile TiO₂, a morphology analysis experiment was conducted against the aging time in the HCl aqueous solution. As displayed in Figures 3a and S3, the as-synthesized pristine product exhibits a distinct nanotube morphology with an outer diameter of approximately 5−10 nm. After being treated with the HCl aqueous solution for 10 days, it is observed from Figure 3b that most of the product retains the one-dimensional structure features similar to those of the parent nanotubes even though the sample undergoes a crystallographic transformation from titanate to anatase. Additionally, it is noted here that small crystal particles with a size of approximately 5 nm were also observed on the surface of the tubular structure, and the HRTEM result (Figure 4b) showed that the granular particle displayed a lattice fringe of 0.35 nm closely matching well with the (101) crystalline plane of the anatase phase. The aforementioned fact that no signal of the intermediate (e.g., TiO₂ (B)) is harvested at the early stage indicates that the transformation from H-titanate to anatase phase TiO₂ happened rapidly and completely. Allowing the system to age for a long time (20 days) led to the further evolution of titanate precursors. As indicated in Figure 3c,d, aside from nanoparticles and nanotube-like structures, a novel spindle-like TiO₂ structure was also observed. The HRTEM images shown in Figure 4c,d demonstrate that the spindle-like structures are exposed to the (110) plane of $d = 0.32$ nm, indicating that the product exists in the form of a rutile phase, which is in agreement with the XRD results shown in Figure 1. What is more, in addition to spindle-like rutile, the anatase and rutile nanocrystals could also be recognized by the characteristic spacing of 0.35 and
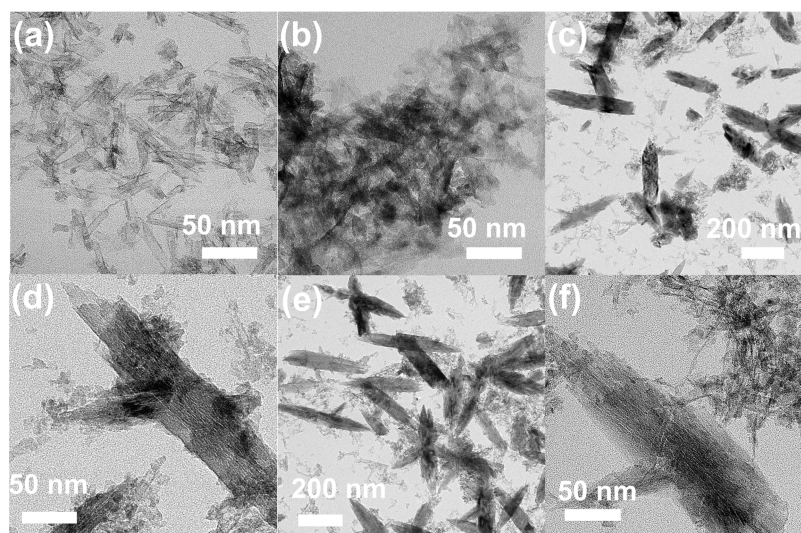

Figure 3. TEM images of TiO₂ products obtained from H-titanate at varied reaction times: (a) 1 day, (b) 10 days, (c, d) 20 days, and (e, f) 40 days.
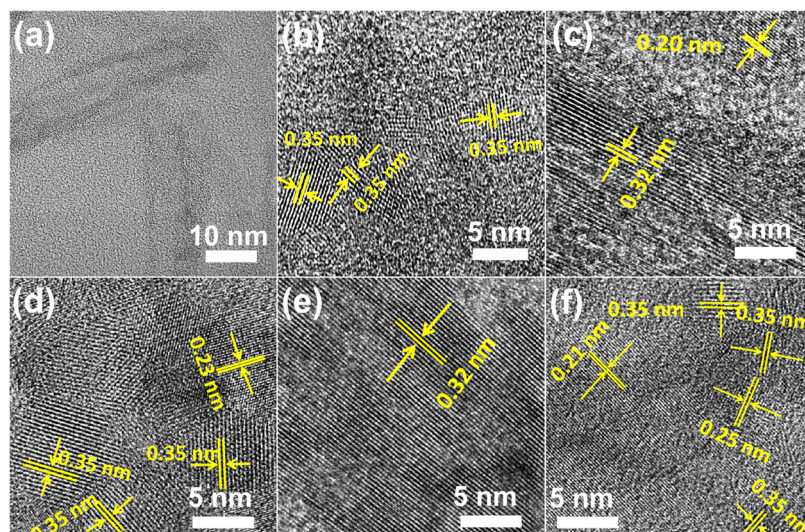
Figure 4. HRTEM images of TiO$_2$ products obtained from H-titanate at varied reaction times: (a) 1 day, (b) 10 days, (c, d) 20 days, and (e, f) 40 days.
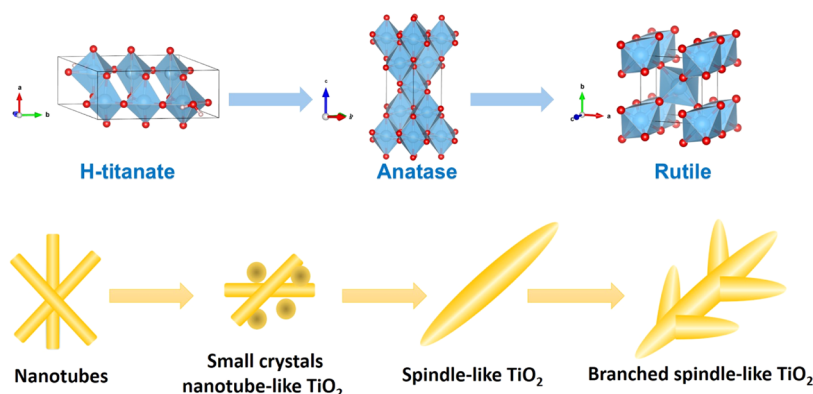

Figure 5. Schematic illustrations of the structures of H-titanate, anatase, and rutile TiO$_2$ and the time-dependent-phase transition process from H-titanate to rutile TiO$_2$ during the aging process. The blue-gray octahedra and blue and red balls represent the TiO$_6$ units and Ti and O atoms, respectively.

0.23 nm indexed to the (101) and (112) planes of anatase and 0.20 nm to the (210) plane of rutile, respectively.[43,44] The formed small crystals could probably act as primary species to construct the elongated particles in a highly oriented fashion. As the reaction time proceeded (40 days), the amount of the hierarchical TiO$_2$ increased continuously along with the gradual decrease of nanoparticles and nanotube-like structures (Figure 3e,f). The above morphology variation also indicates that the formation of hierarchical TiO$_2$ was at the expense of small nanoparticle structures synthesized in the foregoing stage, during which nanoparticles and nanotube-like structures acted as precursors and sacrificed themselves to form hierarchical TiO$_2$. It can also be concluded that, by comparing Figure 3e with Figure 2a, when the reaction time is long enough, both the granular particles and tubular-like structures could be completely converted into the branched 3D architecture.

3.3. Mechanism for HTs Formation. Based on the above experimental findings, a most plausible transformation mechanism is tentatively proposed to illustrate the transformation from titanate nanotubes to 3D branched hierarchical rutile TiO$_2$, as displayed in Figure 5. The transition started with the dehydration of the H-titanate nanotubes, followed by

the rearrangement for the formation of the anatase structure via an in situ topotactic structural transformation reaction.[39] Typically, in the early stage, the titanate precursor dehydrated, while most of the large structural units such as zigzag ribbons were almost unchanged, and the anatase phase was formed by rearranging the crystal lattice with the nanotube-like structure retained. In addition, the titanate could also convert to anatase crystals via a dissolution/recrystallization mechanism, during which the titanates proceed with rupture and dissolution, followed by recrystallization, as a result of local shrinkage of the titanate on the tube wall, probably driven by releasing the strong stress and reducing the total energy during the process.[45] Different from titanate and anatase, rutile is composed of the linkage of the linear TiO$_6$ chains derived from the two edges sharing a TiO$_6$ octahedron. Therefore, the construction of rutile is most likely to have started from the reconstruction of the lattice. It has been proposed that the zigzag ribbons in anatase will resolve into detached TiO$_6$ octahedra or their small clusters when the driving force (e.g., the acid concentration) is enlarged, followed by the construction of the straight chains by sharing the corner with each other.[36] In our experiment, the proton concentration of the solution changed gradually during the aging time because

of the partial evaporation of the distilled water (see Figure S4). During the process, the previously formed primary anatase crystals would dissolve first into the metastable phase, followed by the nucleation in a highly oriented fashion and growth into rutile by an oriented attachment and Ostwald ripening process.[46] This speculation and observation are also consistent with the common view that the phase transition to rutile always preferentially occurs in a more acidic environment.

Apart from the synthesis of the spindle-like substrate, under the acidic condition, the detached TiO_6 octahedron derived from the dissolution of TiO_2 species could also migrate to the surface of spindle-like substrates and be absorbed on the energetically favorable sites as seeds, followed by the rearrangement into branch shapes with the rutile phase. As shown in Figure S5, the spindle-like structure formed at the initial stage may possess a rough surface and expose more defects on the surface, thus providing certain sites for the growth of the TiO_2 branches.[47] Moreover, the same crystal plane (i.e., (110) plane) and the orientation (i.e., along the [001] axis) for both branches and substrates may also indicate that the two sections are produced via the identical mechanism. The difference lies in the fact that the nucleation and growth of the branches only occurred selectively at some favorable locations rather than the whole surface of the substrates.

3.4. N$_2$ Adsorption−Desorption Isotherms and UV−Vis Absorption Spectra.
To better understand the designed novel photoanode material, the N_2 adsorption−desorption isotherms and UV−vis absorption spectra measurements were recorded. As demonstrated in Figure 6a, the adsorbing amount
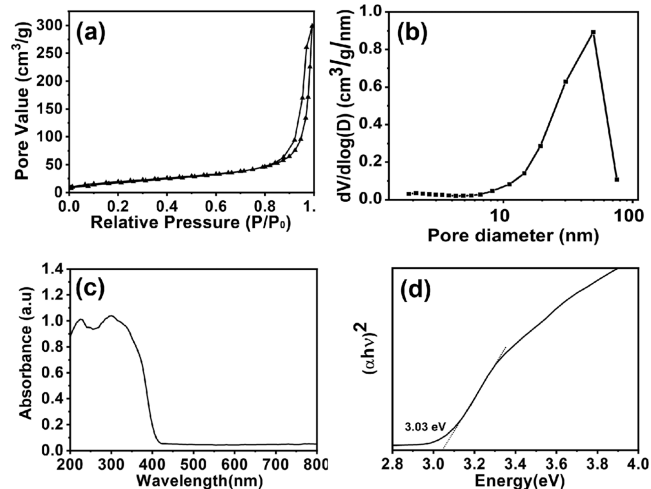

Figure 6. (a) N_2 adsorption−desorption isotherms, (b) pore size distribution, (c) UV−vis light absorption spectra, and (d) estimated band gap of HTs.

of the as-prepared TiO_2 nanostructure rises very steeply at higher pressures, indicating the presence of capillary condensation of N_2 in the mesopores or macropores. Further observation reveals that the hysteresis loops do not level off even at the pressures approaching the saturation vapor pressure, demonstrating the presence of slitlike pores.[48,49] This conclusion is in good agreement with the BJH pore size distributions of HTs shown in Figure 6b. Additionally, by comparing the absorption amount of N_2 on both HTs and P25, it can be found that the N_2 adsorption on HTs is obviously higher than that of the commercial P25 TiO_2 (see Figure S6a).

The specific calculation shows that HTs exhibit a high total cumulative pore volume of 0.46 cm^3 g^{-1}, approximately 2.5 times larger than that of the commercial TiO_2 (P25, 0.19 cm^3 g^{-1}). Such structural features finally endow the HTs sample with a high specific surface area of 76.9 m^2 g^{-1}, obviously higher than that of P25 (51.2 cm^3 g^{-1}). The characteristic pore structure, higher pore value, and larger surface area of the as-synthesized HTs could be favorable for electrolyte percolation within the film and dye sensitizer absorption on the resultant photoanode.

The UV−vis diffuse reflectance spectrum was also investigated to get more insight into the HTs powder. As shown in Figure 6c, HTs demonstrate an absorption edge of approximately 413 nm, which is a little larger than that of the raw material P25 (see Figure S6b). The slight shift of the whole absorption edge toward the low energy implies the difference in the intrinsic band gap between the samples. The band gap (E_g) of the as-prepared HTs is calculated on the basis of the Kubelka−Munk equation, $(\alpha h\nu)^2 = k(h\nu - E_g)$, where α and $h\nu$ are the absorption coefficient and photon energy, respectively, while E_g and A are the band gap and Tauc's constant, respectively.[50] As displayed in Figure 6d, the E_g value of the HTs sample estimated by the intersection of the tangent line with the $h\nu$-axis, i.e., the extrapolated intercept, is about 3.03 eV, which further demonstrates that the as-prepared sample is the rutile structure.

3.5. Photovoltaic Performance of HTs Photoanodes.
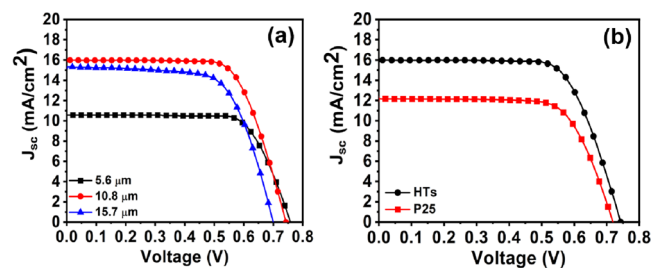As shown in Figure 7a and Table 1, the J_{SC} evolves from 10.5

Figure 7. (a) $J−V$ curves of the cells based on HTs with different thicknesses and (b) the $J−V$ characteristic comparison of HTs and P25.

Table 1. Characteristics of the Hierarchically Branched TiO$_2$ Photoanodes with Different Thickness Together with the Corresponding Photovoltaic Parameters

| thickness	J_{SC} (mA cm^{-2})	V_{OC} (V)	FF (%)	PCE
5.6	10.5	0.757	73.5	5.88
10.8	16.0	0.743	69.5	8.32
157	15.3	0.700	66.7	7.15

to 16.0 mA cm^{-2} for HTs-1 to HTs-2 along with increasing film thickness from 5.6 to 10.8 μm and then drops to 15.3 mA cm^{-2} as the film thickness is creased 15.7 μm. In contrast to J_{SC}, the open-circuit voltage decreases gradually from HTs-1 to HTs-3 with the film thickness increment. As reported previously, the increase of film thickness will lead to the change of several features of the resultant photoanodes including the charge recombination sites, dye uptakes, electron transfer rate, and even electronic band position, which consequently exert synergistic influence on the characteristic parameters of cells and thereafter cause different variation tendency.[51]

Table 2. Comparison of the Characteristics of HTs and the Reference P25-Based Photoanodes Together with Their Corresponding Photovoltaic Parameters

sample	S_{BET} (m^2 g^{-1})	J_{SC} (mA cm^{-2})	V_{OC} (V)	FF	PCE	adsorbed dye [$\times10^{-7}$ mol cm^{-2}]
HTs	76.9	16.0	0.743	70	8.32	3.38
P25	51.2	12.0	0.712	70	5.97	2.53

In this study, P25 TiO$_2$, a conventional TiO$_2$ nanoparticle with a 0D structure, was selected as the starting material for the preparation of the 3D HTs. Considering the relationship between the two materials and their feature differences, P25 TiO$_2$ was thus chosen as the reference to make a comparison with the as-prepared novel HTs, which, we believe, is more favorable to indicate the virtues of the designed product. The recorded current−voltage (J−V) curves of both DSCs are depicted in Figure 7b, and their corresponding photovoltaic characteristics, including the directly recorded short-circuit current density (J_{SC}), open-circuit voltage (V_{OC}), fill factor (FF), and overall photoelectric conversion efficiency (PCE) calculated from the J−V curves, are summarized in Table 2. It is seen that the reference cell only displays a low efficiency of 5.97% with a V_{OC} of 0.712 V and a J_{SC} of 12.0 mA cm^{-2}. In contrast, a higher V_{OC} of 0.743 V and J_{SC} of 16.0 mA cm^{-2} are delivered for the desired HTs cells, thereby resulting in an encouraging PCE of 8.32%, surpassing most of the previously reported hierarchical rutile TiO$_2$ (see Table S1). The observed photovoltaic performance enhancement is undisputed to be related to the unique morphological feature of HTs, which will be experimentally investigated in the following sections, as displayed below.

3.6. Dye Absorption and Reflectance Spectra of the HTs Photoanodes. To elucidate the difference in the DSC performance, the dye loading capabilities of the resulting photoanodes were first compared (see Figure 8a). Note that in
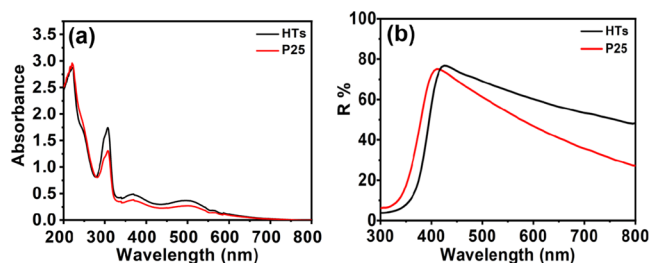

Figure 8. (a) UV−vis spectra of the dye solution desorbed from the photoanode films and (b) diffused reflectance spectra based on HTs and P25.

comparison with that of the commercial P25, the HTs film exhibited a much better ability in dye adsorption, with the calculated dye anchoring amount reaching up to 3.38 × 10^{-7} mol cm^{-2}, higher than that of the P25 TiO$_2$ film, which merely showed an absorbed dye amount of 2.53 × 10^{-7} mol cm^{-2}. The obvious increment of the dye attachment could be due to the distinct augment of the overall surface area of the HTs film, as verified by the BET specific surface area (S_{BET}) measurements (see Table 2). The increased dye loading amount is beneficial to the sufficient capturing of the incident photons and, thus, brings about a larger short-circuit current density.

The influence of particular morphological features on the light-harvesting capability also reflects on the change of scattering properties of the resultant photoanode. As is reported that whether the incident light is harvested by the

film or transmitted through the photoanode film directly depends on the structure of the photoanode material.[52,53] Hierarchical structure composed of various building blocks could be an ideal candidate for the photoanode material for substantially improving the light-scattering performance. As expected, from the UV−vis reflectance spectroscopy shown in Figure 8b, it can be seen that the well-designed HTs photoanode exhibits a stronger reflectance capability within a wild wavelength region from 400 to 800 nm in comparison with the commercially-obtained TiO$_2$ film. This observation here implies that more input photons will be harvested by the sensitizer molecules adsorbed to the photoanode surface.

3.7. EIS Analysis. To better understand the appreciable electron transport properties of the resulting HTs-based DSCs, electrochemical impedance spectroscopy (EIS) measurements were performed at V_{OC} under light irradiation, as shown in Figure 9a. Three distinguishable semicircles corresponding to
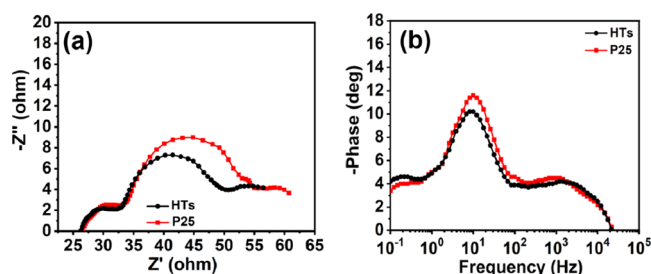
Figure 9. (a) Nyquist and (b) Bode plots of DSCs based on HTs and P25.

the electrochemical reaction that occurred at the counter electrode, the dye-sensitized photoanode film electrolyte interface, and the Warburg diffusion process were observed in the sequence from left to right.[54,55] Typically, the prominent middle semicircle in the range of 10^0−10^3 Hz can be used to estimate the extent of electron transport in the photoanode film according to the diameter of the specific semicircle. As can be seen, a smaller diameter is obtained for the HTs electrode, indicating a decreased impedance and accelerated electron transport ability in the designed HTs photoelectrode. Such a change in the interface charge transfer resistance further indicates the structural advantage of hierarchical TiO$_2$. The corresponding Bode phase plots drawn from the Nyquist plots are given in Figure 9b, and two frequency peaks located at the intermediate frequency region of 10^0−10^2 Hz and a high-frequency regime of 10^3−10^4 Hz are observed, respectively. The electron lifetime (τ_e) in the resultant HTs-based cells is related to the maximum value (f_{max}) of the middle-frequency peak mentioned above and can be acquired using the equation of $\tau = 1/\omega_{max} = 1/2\pi f_{max}$. The calculated electron lifetime of the HTs photoanode is 18.5 ms, which is remarkably larger than that of commercial TiO$_2$ (14.9 ms). The prolonged electron lifetime could be derived from the higher electron mobility through the hierarchical rutile TiO$_2$ structure.

3.8. IPCE Spectra. The typical IPCE spectra as a function of the illuminated wavelength for the representative HTs-based device are plotted in Figure 10. Clearly, strong photoactivity
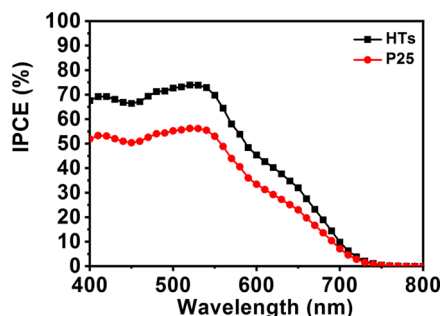

Figure 10. Incident photon-to-current conversion efficiency (IPCE) curves of HTs and P25-based DSCs.

for both of the manufactured photoanodes is shown in the wavelength range from 400 to 750 nm. In contrast to the reference cell, the hierarchical TiO_2 configuration shows an impressively higher photoresponse across almost the entire visible light range from 400 to 800 nm. This phenomenon is also in good agreement with the photocurrent action spectra displayed in Figure 3, where a higher J_{SC} of HTs cells is observed. It is generally accepted that IPCE is predominantly determined by the incident light-harvesting efficiency, the charge carrier collection efficiency, and the injection efficiency of electrons from the excited dye into TiO_2. The first two factors are dictated by the amount of dye absorbed and the capacity for electron transport, respectively, while the third is, in turn, governed by the locations of the excited states of the dye and the titania conduction band.[56,57] In this work, the two types of cells fabricated had very different dye absorption capacities, with HTs having a significantly larger sensitizer loading amount than the reference TiO_2. The variation in dye sensitizer absorption will directly cause a change in incident light-harvesting efficiency, which ultimately makes a considerable difference in the IPCE. On the other hand, as opposed

to irregular nanoparticles, the regular 1D substrate and branches in HTs photoanodes could provide direct paths for fast electron transport (see Figure 11), reducing the amount of undesirable charge recombination and accelerating electron diffusion within the film, which inevitably improved the charge collection efficiency. As the rutile phase has a more positive conduction band edge potential, electron injection from the dye into the TiO_2 conduction band may be favored due to a strong driving force for charge injection, leading to an improved injection yield. As such, the synergistic effect of all of the aforementioned traits in relation to their physical and structural qualities may be the cause of the greater IPCE for HTs.

4. CONCLUSIONS

In summary, we described a novel method for processing the H-titanate nanotube precursor at room temperature to create a fascinating hierarchical rutile TiO_2 architecture with spindle-like substrates and branches. During the reaction process, successive crystal phase transitions from the H-titanate precursor to anatase and subsequently rutile were seen, along with the puzzling evolution of the shape from nanotube to spindle-like hierarchical structures. Due to the high synthetic flexibility of the newly created revolutionary wet-chemical reaction method, it is simple to scale up the synthesis process and greatly expand the composition and morphological tailoring pathway. In an attempt to construct the photoanode, the as-prepared TiO_2 hierarchical structure was made, and an overall power conversion efficiency of 8.32% was attained, which represented an improvement of around 40% over the commercial TiO_2 (P25) used in the experiment. Such a remarkable efficiency enhancement could be the result of the synergetic effect of beneficial properties of a high surface area, improved light scattering, and fast electron transport.

■ ASSOCIATED CONTENT

ⓢ Supporting Information

The Supporting Information is available free of charge at https://pubs.acs.org/doi/10.1021/acsomega.2c06432.
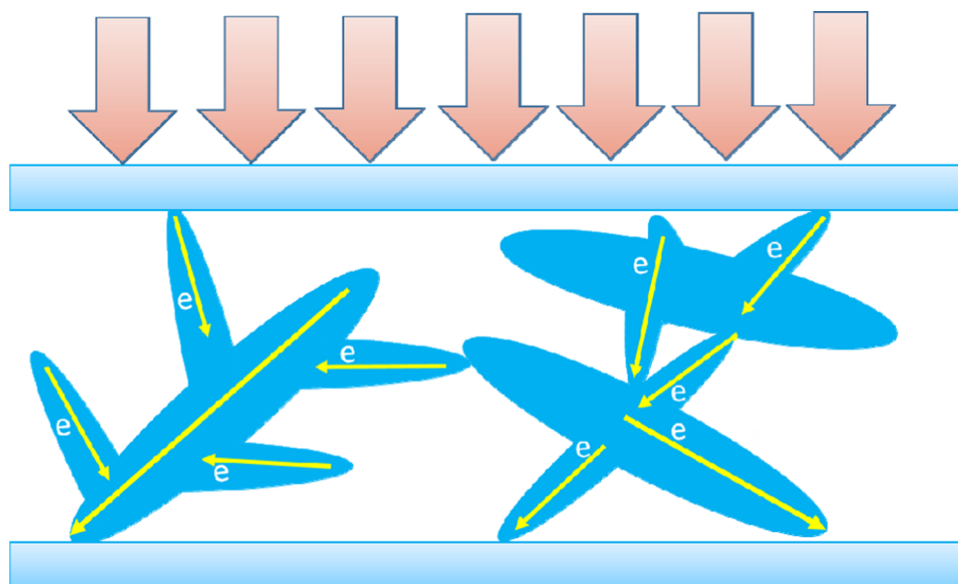

Figure 11. Schematic illustration of electron (e^-) diffuse transport in the HTs-based photoanode film.

XRD patterns of the samples obtained after being calcined at a high temperature and treated at a low concentration, HRTEM images of HTs, variation of the pH value of the solution during the aging process, SEM images of the sample treated for 40 days, and N_2 adsorption−desorption isotherms of P25 (PDF)

■ AUTHOR INFORMATION

Corresponding Author

Dongting Wang − *Shandong Provincial Key Laboratory of Chemical Energy Storage and Novel Cell Technology, School of Chemistry and Chemical Engineering, Liaocheng University, Liaocheng 252059, China;* ⊙ orcid.org/0000-0002-5350-6027; Email: zhangzl@zjut.edu.cn

Authors

Yifan Hu − *Shandong Provincial Key Laboratory of Chemical Energy Storage and Novel Cell Technology, School of Chemistry and Chemical Engineering, Liaocheng University, Liaocheng 252059, China*

Yuchen Li − *Shandong Provincial Key Laboratory of Chemical Energy Storage and Novel Cell Technology, School of Chemistry and Chemical Engineering, Liaocheng University, Liaocheng 252059, China*

Xiangchen Jia − *Shandong Provincial Key Laboratory of Chemical Energy Storage and Novel Cell Technology, School of Chemistry and Chemical Engineering, Liaocheng University, Liaocheng 252059, China*

Yuzhen Fang − *Shandong Provincial Key Laboratory of Chemical Energy Storage and Novel Cell Technology, School of Chemistry and Chemical Engineering, Liaocheng University, Liaocheng 252059, China;* Present Address: Y.F.: Department of Chemical Engineering, Renai College of Tianjin, Tianjin 301636, P. R. China

Zhiliang Zhang − *College of Chemical Engineering, Zhejiang University of Technology, Hangzhou 310014, China*

Xianxi Zhang − *Shandong Provincial Key Laboratory of Chemical Energy Storage and Novel Cell Technology, School of Chemistry and Chemical Engineering, Liaocheng University, Liaocheng 252059, China*

Complete contact information is available at:
https://pubs.acs.org/10.1021/acsomega.2c06432

Notes

The authors declare no competing financial interest.

■ REFERENCES

(1) Song, D. D.; Cui, P.; Wang, T.; Xie, B.; Jiang, Y.; Li, M.; Li, Y.; Du, S.; He, Y.; Liu, Z.; Mbebgue, J. M. Bunchy TiO2 hierarchical spheres with fast electron transport and large specific surface area for highly efficient dye-sensitized solar cells. *Nano Energy* **2016**, *23*, 122−128.

(2) Grätzel, M. Photoelectrochemical cells. *Nature* **2001**, *414*, 338−344.

(3) Ren, H.; Shao, H.; Zhang, L. J.; Guo, D.; Jin, Q.; Yu, R. B.; Wang, L.; Li, Y. L.; Wang, Y.; Zhao, H. J.; Wang, D. A. A New

Graphdiyne Nanosheet/Pt Nanoparticle-Based Counter Electrode Material with Enhanced Catalytic Activity for Dye-Sensitized Solar Cells. *Adv. Energy Mater.* **2015**, *5*, No. 1500296.

(4) Yi, L. X.; Liu, Y. Y.; Yang, N. L.; Tang, Z. Y.; Zhao, H. J.; Ma, G. H.; Su, Z. G.; Wang, W. One dimensional cuins2−Zns heterostructured nanomaterials as low-cost and high-performance counter electrodes of dye-sensitized solar cells. *Energy Environ. Sci.* **2013**, *6*, 835−840.

(5) Wang, D. T.; Yang, H. Z.; Bai, X.; Xing, Y. R.; Hu, X.; Su, J. Q.; Xu, Z. Q.; Ye, X. Y.; Bi, S. Q.; Zhang, X. X.; Fang, Y. Z.; Zhao, J. S. Highly crystallized c-doped nickel oxide nanoparticles for p-type dye-sensitized solar cells with record open-circuit voltage breaking 0.5 v. *Ind. Eng. Chem. Res.* **2020**, *59*, 175−182.

(6) Yu, H.; Pan, J.; Bai, Y.; Zong, X.; Li, X.; Wang, L. Z. Hydrothermal synthesis of a crystalline rutile TiO2 nanorod based network for efficient dye-sensitized solar cells. *Chem. - Eur. J.* **2013**, *19*, 13569−13574.

(7) He, X.; Liu, J.; Zhu, M.; Guo, Y.; Ren, Z.; Li, X. Preparation of hierarchical rutile TiO2 microspheres as scattering centers for efficient dye-sensitized solar cells. *Electrochim. Acta* **2017**, *255*, 187−194.

(8) Li, H. L.; Yu, Q.; Huang, J.; Yu, Y. W.; Li, C. L.; Wang, R. Z.; Guo, J. H.; Jiao, F. Y.; Gao, S. J.; Zhang, S. Y.; Zhang, X.; Wang, Y. P.; Wang, P.; Zhao, L. C. Ultralong rutile TiO2 nanowire arrays for highly efficient dye-sensitized solar cells. *ACS Appl. Mater. Interfaces* **2016**, *8*, 13384−13391.

(9) Lin, J.; Heo, Y. U.; Nattestad, A.; Sun, Z.; Wang, L.; Kim, J. H.; Dou, S. X. 3D hierarchical rutile TiO2 and metal-free organic sensitizer producing dye-sensitized solar cells 8.6% conversion efficiency. *Sci. Rep.* **2014**, *4*, No. 5769.

(10) Park, N. G.; Schlichthörl, G.; Lagemaat, J. V. D.; Cheong, H. M.; Mascarenhas, A.; Frank, A. J. Dye-sensitized TiO2 solar cells: structural and photoelectrochemical characterization of nanocrystalline electrodes formed from the hydrolysis of TiCl4. *Chem. J. Phys. B* **1999**, *103*, 3308−3314.

(11) Roh, D. K.; Chi, W. S.; Jeon, H.; Kim, S. J.; Kim, J. H. High efficiency solid state dye-sensitized solar cells assembled with hierarchical anatase pine tree-Like TiO2 nanotubes. *Adv. Funct. Mater.* **2014**, *24*, 379−386.

(12) Sayahi, H.; Aghapoor, K.; Mohsenzadeh, F.; Morad, M. M.; Darabi, H. R. TiO2 nanorods integrated with titania nanoparticles: large specific surface area 1D nanostructures for improved efficiency of dye-sensitized solar cells (DSSCs). *Solar Energy* **2021**, *215*, 311−320.

(13) Wan, J. S.; Li, T.; Wang, B. Y.; Zhang, J.; Wang, H.; Lund, P. D. A facile method to produce TiO2 nanorods for high-efficiency dye solar cells. *J. Power Sources* **2019**, *438*, No. 227012.

(14) Wu, W. Q.; Xu, Y. F.; Su, C. Y.; Kuang, D. B. Ultra-long anatase TiO2 nanowire arrays with multi-layered configuration on FTO glass for high efficiency dye-sensitized solar cells. *Energy Environ. Sci.* **2014**, *7*, 644−649.

(15) Roh, D. K.; Chi, W. S.; Ahn, S. H.; Jeon, H.; Kim, J. H. One-step synthesis of vertically aligned anatase thornbush-like TiO2 nanowire arrays on transparent conducting oxides for solid-state dye-sensitized solar cells. *Chemsuschem* **2013**, *6*, 1384−1391.

(16) Mustafa, M. N.; Shafie, S.; Wahid, M. H.; Sulaiman, Y. Light scattering effect of polyvinyl-alcohol/titanium dioxide nanofibers in the dye-sensitized solar cell. *Sci. Rep.* **2019**, *9*, No. 14952.

(17) Roh, D. K.; Chi, W. S.; Jeon, H.; Kim, S. J.; Kim, J. H. High efficiency solid state dye-sensitized solar cells assembled with hierarchical anatase pine tree-like TiO2 nanotubes. *Adv. Funct. Mater.* **2014**, *24*, 379−386.

(18) Jiang, L.; Sun, L.; Yang, D.; Zhang, J.; Li, Y. J.; Zou, K.; Deng, W. Q. Niobium-doped (001)-dominated anatase TiO2 nanosheets as photoelectrode for efficient dye-sensitized solar cells. *ACS Appl. Mater. Interfaces* **2017**, *11*, 9576−9583.

(19) Borbón, S.; Lugo, S.; Pourjafari, D.; Aguilar, N. P.; Oskam, G.; López, I. Open-circuit voltage (VOC) enhancement in TiO2-based DSSCs: incorporation of ZnO nanoflowers and Au nanoparticles. *ACS Omega* **2020**, *19*, 10977−10986.

(20) Lin, J. J.; Heo, Y. U.; Nattestad, A.; Shahabuddin, M.; Yamauchi, Y.; Kim, J. H. N719- and D149-sensitized 3D hierarchical rutile TiO2 solar cells-a comparative study. *Phys. Chem. Chem. Phys.* **2015**, *17*, 7208−7213.

(21) Ye, M.; Liu, H. Y.; Lin, C. J.; Lin, Z. Q. Hierarchical rutile TiO2 flower cluster-based high efficiency dye-sensitized solar cells via direct hydrothermal growth on conducting substrates. *Small* **2013**, *9*, 312−321.

(22) Zhang, J. Y.; He, X.; Zhu, M. H.; Guo, Y.; Li, X. The preparation of hierarchical rutile TiO2 microspheres constructed with branched nanorods for efficient dye-sensitized solar cells. *J. Alloys Compd.* **2018**, *747*, 729−737.

(23) Yu, Y. H.; Li, J.; Geng, D. L.; et al. Development of lead iodide perovskite solar cells using three-dimensional titanium dioxide nanowire architectures. *ACS Nano* **2015**, *9*, 564−572.

(24) Yang, B.; Mahjouri-Samani, M.; Rouleau, C. M.; Geohegana, D. B.; Xiao, K. Low temperature synthesis of hierarchical TiO2 nanostructures for high performance perovskite solar cells by pulsed laser deposition. *Phys. Chem. Chem. Phys.* **2016**, *18*, 27067−27072.

(25) Khalily, M. A.; Eren, H.; Akbayrak, S.; Susapto, H. H.; Biyikli, N.; Özkar, S.; Guler, M. O. Facile synthesis of three-dimensional Pt-TiO2 nano-networks: a highly active catalyst for the hydrolytic dehydrogenation of ammonia−borane. *Angew. Chem.* **2016**, *128*, 12445−12449.

(26) Wang, D. A.; Zhang, L. B.; Lee, W.; Knez, M.; Liu F, L. Novel three-dimensional nanoporous alumina as a template for hierarchical TiO2 nanotube arrays. *Small* **2013**, *9*, 1025−1029.

(27) Zhuge, F. W.; Qiu, J. J.; Li, X. M.; Gao, X. D.; Gan, X. Y.; Yu, W. D. Toward hierarchical TiO2 nanotube arrays for efficient dye-sensitized solar cells. *Adv. Mater.* **2011**, *23*, 1330−1334.

(28) Mahmood, K.; Swain, B. S.; Amassian, A. Highly efficient hybrid photovoltaics based on hyperbranched three-dimensional TiO2 electron transporting materials. *Adv. Mater.* **2015**, *27*, 2859−2865.

(29) Liu, Y. Y.; Wang, Y. L.; Ye, X. Y.; Qiao, X. D.; Luo, Q. P.; Lei, B. X.; Sun, W.; Sun, Z. F. Ultra-long hierarchical bud-like branched TiO2 nanowire arrays for dye-sensitized solar cells. *Thin Solid Films.* **2017**, *640*, 14−19.

(30) Wang, H.; Bai, Y.; Wu, Q.; Zhou, W.; Zhang, H.; Li, J. H.; Guo, L. Rutile TiO2 nano-branched arrays on FTO for dye-sensitized solar cells. *Phys. Chem. Chem. Phys.* **2011**, *13*, 7008−7013.

(31) Nakahira, A.; Kubo, T.; Numako, C. TiO2-derived titanate nanotubes by hydrothermal process with acid treatments and their microstructural evaluation. *ACS Appl. Mater. Interfaces* **2010**, *2*, 2611−2616.

(32) Du, G. H.; Chen, Q.; Che, R. C.; Yuan, Z. Y.; Peng, L. M. Preparation and structure analysis of titanium oxide nanotubes. *Appl. Phys. Lett.* **2001**, *79*, 3702−3704.

(33) Kasuga, T. D.; Hiramatsu, M.; Hoson, A.; Sekino, T.; Niihara, K. Titania nanotubes prepared by chemical processing. *Adv. Mater.* **1999**, *11*, 1307−1310.

(34) Kiatkittipong, K.; Scott, J.; Amal, R. Hydrothermally synthesized titanate nanostructures: impact of heat treatment on particle characteristics and photocatalytic properties. *ACS Appl. Mater. Interfaces* **2011**, *3*, 3988−3996.

(35) Vijayan, B.; Dimitrijevic, N. M.; Rajh, T.; Gray, K. Effect of calcination temperature on the photocatalytic reduction and oxidation processes of hydrothermally synthesized titania nanotubes. *J. Phys. Chem. C* **2010**, *114*, 12994−13002.

(36) Liu, Y. X.; Wang, Z. L.; Wang, W. D.; Huang, W. X. Engineering highly active TiO2 photocatalysts via the surface-phase junction strategy employing a titanate nanotube precursor. *J. Catal.* **2014**, *310*, 16−23.

(37) Tsai, C. C.; Teng, H. Nanotube formation from a sodium titanate powder via low-temperature acid treatment. *Langmuir* **2008**, *24*, 3434−3438.

(38) Kiatkittipong, K.; Ye, C.; Scott, J.; Amal, R. Understanding hydrothermal titanate nanoribbon formation. *Cryst. Growth Des.* **2010**, *10*, 3618−3625.

(39) Wang, H. K.; Shao, W.; Gu, F.; Zhang, L.; Lu, M. K.; Li, C. Z. Synthesis of anatase TiO2 nanoshuttles by self-sacrificing of titanate nanowires. *Inorg. Chem.* **2009**, *48*, 9732−9736.

(40) Zhu, H. Y.; Gao, X. P.; Lan, Y.; Song, D. Y.; Xi, Y. X.; Zhao, J. C. Hydrogen titanate nanofibers covered with anatase nanocrystals: a delicate structure achieved by the wet chemistry reaction of the titanate nanofibers. *J. Am. Chem. Soc.* **2004**, *126*, 8380−8381.

(41) Zhu, H. Y.; Lan, Y.; Gao, X. P.; Ringer, S. P.; Zheng, Z. F.; Song, D. Y.; Zhao, J. C. Phase transition between nanostructures of titanate and titanium dioxides via simple wet-chemical reactions. *J. Am. Chem. Soc.* **2005**, *127*, 6730−6736.

(42) Oh, J. K.; Lee, J. K.; Kim, H. S.; Han, S. B.; Park, K. W. TiO2 branched nanostructure electrodes synthesized by seeding method for dye-sensitized solar cells. *Chem. Mater.* **2010**, *22*, 1114−1118.

(43) Yang, W. X.; Hou, H. L.; Yang, Y.; Ma, G. Z.; Zhan, X. Q.; Yang, H. L.; Yang, W. Y. MXene-derived anatase-TiO2/rutile-TiO2/In2O3 heterojunctions toward efficient hydrogen evolution. *Colloids Surf., A* **2022**, *652*, No. 129881.

(44) Li, G. J.; Huang, J. Q.; Xue, C. B.; Chen, J.; Deng, Z. H.; Huang, Q. F.; Liu, Z. G.; Gong, C.; Guo, W.; Cao, R. Facile synthesis of oriented feather-like TiO2 bundle catalysts for efficient photocatalytic water splitting. *Cryst. Growth Des.* **2019**, *19*, 3584−3591.

(45) Wang, J. Y.; Han, X. J.; Liu, C.; Zhang, W.; Cai, R. X.; Liu, Z. H. Adjusting the crystal phase and morphology of titania via a soft chemical process. *Cryst. Growth Des.* **2010**, *10*, 2185−2191.

(46) Shin, H.; Jung, H. S.; Hong, K. S.; Lee, J. K. Crystal phase evolution of TiO2 nanoparticles with reaction time in acidic solutions studied via freeze-drying method. *J. Solid State Chem.* **2005**, *178*, 15−21.

(47) Ye, M.; Zheng, D. J.; Wang, M. Y.; Chen, C.; Liao, W. M.; Lin, C. J.; Lin, Z. Q. Hierarchically structured microspheres for high-efficiency rutile TiO2-based dye-sensitized solar cells. *ACS Appl. Mater. Interfaces* **2014**, *6*, 2893−2901.

(48) An, T. C.; Liu, J. K.; Li, G. Y.; Zhang, S. Q.; Zhao, H. J.; Zeng, X. Y.; Sheng, G. Y.; Fu, J. M. Structural and photocatalytic degradation characteristics of hydrothermally treated mesoporous TiO2. *Appl. Catal., A* **2008**, *350*, 237−243.

(49) Kruk, M.; Jaroniec, M. Gas adsorption characterization of ordered organic−inorganic nanocomposite materials. *Chem. Mater.* **2001**, *13*, 3169−3183.

(50) Patel, M.; Chavda, A.; Mukhopadhyay, I.; Kim, J.; Ray, A. Nanostructured SnS with inherent anisotropic optical properties for high photoactivity. *Nanoscale* **2016**, *8*, 2293−2303.

(51) Guo, D. P.; Xiao, S. Q.; Fan, K.; Yu, J. G. Hierarchical TiO2 submicrorods improving photovoltaic performance of dye-sensitized solar cells. *ACS Sustainable Chem. Eng.* **2017**, *5*, 1315−1321.

(52) Bai, Y.; Xing, Z.; Yu, H.; Li, Z.; Amal, R.; Wang, L. Z. Porous titania nanosheet/nanoparticle hybrids as photoanodes for dye-sensitized solar cells. *ACS Appl. Mater. Interfaces* **2013**, *5*, 12058−12065.

(53) Wang, D. T.; Liu, S. H.; Shao, M.; Li, Q.; Gu, Y.; Zhao, J.; Zhang, X.; Zhao, J.; Fang, Y. Aqueous solution-processed multifunctional SnO2 aggregates for highly efficient dye-sensitized solar cells. *Ind. Eng. Chem. Res.* **2018**, *57*, 7136−7145.

(54) Zheng, Y. Z.; Tao, X.; Hou, Q.; Wang, D. T.; Zhou, W. L.; Chen, J. F. Iodine-doped ZnO nanocrystalline aggregates for improved dye-sensitized solar cells. *Chem. Mater.* **2011**, *23*, 3−5.

(55) Zhang, X. L.; Huang, F.; Nattestad, A.; Wang, K.; Fu, D.; Mishra, A.; Bauerle, P.; Bach, U.; Cheng, Y. B. Enhanced open-circuit voltage of p-type DSC with highly crystalline NiO nanoparticles. *Chem. Commun.* **2011**, *47*, 4808−4810.

(56) Yella, A.; Lee, H. W.; Tsao, H. N.; Yi, C.; Chandiran, A. K.; Nazeeruddin, M. K.; Diau, W. G.; Yeh, C. Y.; Zakeeruddin, S. M.; Grtzel, M. Porphyrin-sensitized solar cells with cobalt (II/III)−based redox electrolyte exceed 12 percent efficiency. *Science* **2011**, *334*, 629−634.

(57) Lu, X. H.; Zheng, Y. Z.; Bi, S. Q.; Wang, Y.; Tao, X.; Dai, L. M.; Chen, J. F. Multidimensional ZnO architecture for dye-sensitized

solar cells with high-efficiency up to 7.35%. *Adv. Energy Mater.* **2014**, *4*, No. 1301802.